

# Large-Deformation Analysis and Experimental Validation of a Flexure-Based Mobile Sensor Node

Jiajie Guo, Kok-Meng Lee, *Fellow, IEEE*, Dapeng Zhu, Xiaohua Yi, and Yang Wang

**Abstract**—This paper presents a new magnetic wall-climbing car as a mobile sensor node for health monitoring and dynamic testing of large civil (ferromagnetic) structures. Unlike traditional design, where the distance between the front and rear wheel pairs is fixed, the electromagnetically driven compliant beam connecting the axles not only offers an effective means to negotiate corners when maneuvering on ferromagnetic surfaces, but also serves as a sensor attachment device. Specifically, this paper presents the design concept of a novel magnetic flexonic mobile node incorporating a compliant beam and permanent magnets, and a 2-D model for simulating the deformed shape of the compliant beam. Simulation results show that there exist consistent relations between input/output displacements and rotation angle for control implementation in sensor attachment and corner negotiation regardless of gravity direction or the critical force for buckling. Experiment results are also provided to validate the theoretical model and compare with the analysis for sensor attachment and corner negotiation.

**Index Terms**—Buckling, compliant mechanism, constraint, flexible (mobile) robot, flexible structure, large deformation, sensor network.

## I. INTRODUCTION

IN recent years, wireless sensor networks have attracted growing interest for the structural health monitoring (SHM) of civil structures [1]. The leap from traditional cable-based sensing systems to wireless sensor networks can significantly reduce installation time/cost, potentially enable dense instrumentation, and bring unprecedented improvements to structural monitoring. As another transformative change to sensor networks, the next revolution is predicted to be the networks of mobile sensor nodes (MSNs) [2]. In a mobile sensor network, each MSN can be a sensor-carrying robot capable of autonomously exploring surroundings and exchanging information with peers through wireless communication. Motivated by these emerging needs, this paper presents a design method for developing flexure-based MSNs [3], [4] for negotiating obstacles (such as

corners and reinforced ridges) while moving on ferromagnetic surfaces for SHM applications [5].

In general, three important factors in designing a wall-climbing robot are adherence, mobility, and flexibility. In [6], the prototype robot was designed with suction cups for adherence to crawl on nonferrous surfaces to inspect aircraft wings and fuselages. Using an induction pin, a magnetic wheeled robot can be easily detached by manipulating the magnetic flux direction [7]. For steel pipe inspection, a magnetic actuator incorporating shape-memory-alloy coils has been developed to move in the complicated environment of pipes [8]. Most existing wheeled robots for similar applications are often designed and analyzed under small deformations to avoid nonlinearity of lateral bending and buckling. While designs based on rigid links/joints simplify analysis, they potentially limit the versatile functionality of a robot. To overcome this difficulty, multiagent networks, such as a self-assembly modular robot [9], provide a flexible architecture, and relevant control methods for coordinated motions have been developed for multiple mobile robots [10], [11]. This paper offers an alternative solution to design compliant structures allowing large deformation to provide flexible manipulation of a wall-climbing robot, and hence, improves mobility and flexibility of an MSN for SHM. While illustrated in the context of an MSN, this design concept can potentially enhance the flexibility of existing modular robots.

Flexible mechanisms, such as joints and compliant mechanisms, can be explored for such purpose. For example, an active pin joint is incorporated in a magnetic wheeled robot for internal piping inspection [12]. Various compliant mechanisms have also been studied for robot development, owing to the advantage of having no relative moving parts, and thus, no contact frictional dissipation [13]–[17]. For commanding robot movements through real-time feedback, control strategies have been developed based on various modeling methods [18] including rigid body motions [19]–[21], vibration modes [22], and finite-element methods (FEMs) [23], [24].

In many compliant mechanisms, flexible beams are used as a fundamental component. For a 2-D beam capable of large deflection under various load conditions, closed-form solutions can be found in [25]; however, expressed in terms of elliptic integrals, these solutions are computationally cumbersome for use in design and real-time control. More recently, a 3-D beam model was developed in [26] and solved through the multiple shooting method (MSM) [27], [28]. Early study concerning the stability and buckling was motivated by structure design and analysis [29], [30]. Given the instability nature of buckling, its occurrence is usually not desirable; as a result, most studies have been concentrated on the critical forces and load-displacement relation of buckling mechanisms [31]. With

Manuscript received October 4, 2010; revised December 14, 2010; accepted December 31, 2010. Date of publication March 10, 2011; date of current version May 4, 2012. Recommended by Technical Editor D. Sun. This work was supported in part by the National Science Foundation under Grant CMMI-0928095 and in part by the Agricultural Technology Research Program.

J. Guo and K.-M. Lee are with the George W. Woodruff School of Mechanical Engineering, Georgia Institute of Technology, Atlanta, GA 30332 USA (e-mail: kokmeng.lee@me.gatech.edu).

D. Zhu, X. Yi, and Y. Wang are with the School of Civil and Environmental Engineering, Georgia Institute of Technology, Atlanta, GA 30332 USA (e-mail: yang.wang@ce.gatech.edu).

Color versions of one or more of the figures in this paper are available online at <http://ieeexplore.ieee.org>.

Digital Object Identifier 10.1109/TMECH.2011.2107579

few exceptions (such as [32], where the postbuckling equilibrium was analyzed), very little study has been conducted on displacement relations in large deflection and buckling analysis of flexible beams.

This paper presents the design concept, model, and analysis of a flexure-based-mechatronic flexonic mobile node (FMN) [3], [4] for maneuvering on ferromagnetic surfaces. In operation, the FMN utilizes large deflection and buckling of a compliant beam enabling it to flexibly negotiate different kinds of obstacles (such as abrupt angle changes) commonly encountered in complex civil structures. The remainder of this paper is organized as follows.

- 1) With the applications, such as [5], in mind, we present here the design concept of a novel magnet-wheeled FMN incorporating a flexible beam to achieve two important functions (sensor attachment and corner negotiation) with a simple mechanism. Besides being designed to negotiate common obstacles encountered in complex civil structures, the compliant beam offers an effective means to attach/detach an accelerometer (onto or from the surface of a structure) for vibration measurements.
- 2) A general quasi-static compliant beam model for simulating 2-D beam deformation is then given. To exploit beam buckling for SHM applications, the work starts from a conventional viewpoint of load-displacement relation, and then evolves to the displacement–displacement relations. As will be shown, these forward and inverse models provide the essential basis for the design and control of a FMN.
- 3) Performed on a prototype FMN developed at Georgia Tech [3], Atlanta, we then discuss experimental results demonstrating three loading scenarios for the compliant beam. The first validates the basic beam model under its own weight and a concentrated load. The second investigates the effect of gravity on the process of attaching a sensor of different weights. The third evaluates the FMN design by examining the torque provided by compliant beam for maneuvering around a corner on ferromagnetic surfaces.

## II. DESIGN CONCEPT OF AN FMN

Fig. 1 illustrates the design concept of an FMN, which consists of four independently driven magnetic wheels housed in two assemblies (front and rear) connected by a compliant beam. Unlike a rigid car frame with a fixed distance between the front and rear axles, the front axle of an FMN can be bent relatively to its rear axle by deforming the compliant beam (with both of its ends fixed on the two rigid bodies at  $P_0$  and  $P_1$ ). This enables the FMN to not only function as an agile locomotion, but also a sensor loader.

In Fig. 1,  $OXYZ$  is a reference frame, where  $X$  is parallel to the plane on which the FMN moves and points in its moving direction, and  $Z$  is normal to the plane. The local coordinate frames “ $xyz$ ” and “ $\xi\eta\zeta$ ” (each with a subscript indicating its location along the beam path length) are defined in the undeformed and deformed configurations, respectively. For examples,  $x_0y_0z_0$  and  $x_1y_1z_1$  are the local coordinate frames at  $P_0$  and  $P_1$  in the unde-

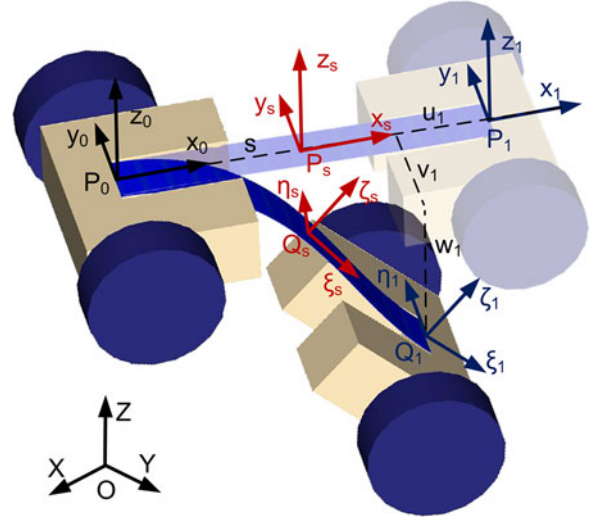


Fig. 1. Design concept and coordinate systems of an FMN.

formed configuration, respectively. Similarly,  $P_s(x_s, y_s, z_s)$  and  $Q_s(\xi_s, \eta_s, \zeta_s)$  represent the same material point to describe the beam shapes before and after deformation, respectively, where the subscript  $s$  denotes the path-length normalized to the beam length  $L$  ( $0 \leq s \leq 1$ ), and  $u_s, v_s,$  and  $w_s$  are the nodal displacements along  $x_s, y_s,$  and  $z_s$  axis directions, respectively. All coordinates follow the right-hand rule with  $x_s$  and  $\xi_s$  assigned along the neutral axis of the beam, and  $z_s$  and  $\zeta_s$  normal to the beam surface.

### A. Beam Deformation Model

Euler–Bernoulli beam theory is adopted to formulate the 2-D large deformation behaviors of the beam subjected to specified forces, moments, and constraints; both point and distributed external loadings are considered. For this, two assumptions are made: 1) the beam material is linear elastic; and 2) cross sections remain planar and normal to the reference axis after deformation. As an illustration, consider an element with length  $\Delta s$  in a compliant beam shown in Fig. 2(a). The element is subjected to two concentrated loads  $F_1$  and  $F_3$ , and a moment  $M_2$ , as well as two external distributed loads  $q_1$  and  $q_3$  and distributed moment  $q_2$ , where the subscripts 1, 2, or 3 corresponds to the  $x, y,$  or  $z$  ( $\xi, \eta,$  or  $\zeta$ ) direction, respectively. In Fig. 2(a), the concentrated loads and moment are presented in the deformed coordinates  $\xi_s, \eta_s,$  and  $\zeta_s$ ; the external distributed loads and moment are in undeformed coordinates  $x_s, y_s,$  and  $z_s$ ; and  $\theta$  is the slope of the deformed beam shape.

Based on static analysis of a beam element, the equations for the force and moment equilibrium are given by (1a)–(1c)

$$-F_1 + (F_1 + \Delta F_1) \cos \Delta\theta + (F_3 + \Delta F_3) \sin \Delta\theta + q_1 \Delta s \cos \theta - q_3 \Delta s \sin \theta = 0 \quad (1a)$$

$$-F_3 + (F_3 + \Delta F_3) \cos \Delta\theta - (F_1 + \Delta F_1) \sin \Delta\theta + q_1 \Delta s \sin \theta + q_3 \Delta s \cos \theta = 0 \quad (1b)$$

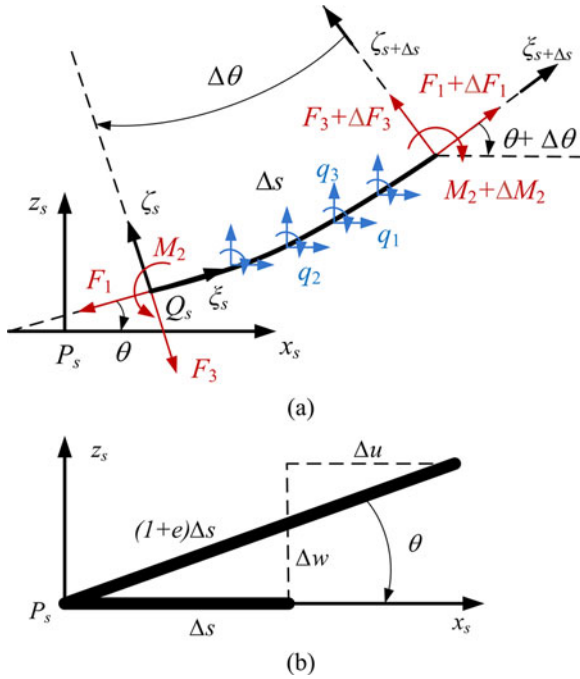


Fig. 2. Formulation of a beam model. (a) Force and moment equilibrium. (b) Displacements and orientation relations.

$$-M_2 + M_2 + \Delta M_2 - (1+e)\Delta s(F_3 + \Delta F_3) + q_1 \Delta s^2/2 - q_3 \Delta s^2/2 + q_2 \Delta s = 0 \quad (1c)$$

where  $e$  is the axial strain. For an infinitesimally small  $\Delta s$ ,  $\sin \Delta \theta \approx \Delta \theta$  and  $\cos \Delta \theta \approx 1$ . Neglecting higher order terms, (1a)–(1c) can be rewritten in differential forms with respect to  $s$

$$F_1' = -F_3 \theta' - q_1 \cos \theta + q_3 \sin \theta \quad (2a)$$

$$F_3' = -F_1 \theta' - q_1 \sin \theta - q_3 \cos \theta \quad (2b)$$

$$M_2' = (1+e)F_3 - q_2. \quad (2c)$$

The element displaces as well as deforms, as illustrated in Fig. 2(b), where  $\Delta s$  and  $[(1+e)\Delta s]$  are the original and deformed element lengths, respectively. From Fig. 2(b), the nodal displacements and orientation can be obtained as follows:

$$\frac{\Delta s + \Delta u}{(1+e)\Delta s} = \cos \theta \quad \frac{\Delta w}{(1+e)\Delta s} = -\sin \theta.$$

These aforementioned relations can be rewritten in differential forms as follows:

$$u' = (1+e) \cos \theta - 1 \quad (3a)$$

$$w' = -(1+e) \sin \theta. \quad (3b)$$

Denoting

$$\theta' = \rho_2 \quad (3c)$$

(2) can be recast as follows:

$$F_1' = -F_3 \rho_2 - q_1 \cos \theta + q_3 \sin \theta \quad (3d)$$

$$F_3' = F_1 \rho_2 - q_1 \sin \theta - q_3 \cos \theta \quad (3e)$$

$$M_2' = (1+e)F_3 - q_2 \quad (3f)$$

where  $e$  and  $\rho_2$  are given by

$$e = \frac{F_1}{EA} \quad (4a)$$

$$\rho_2 = \frac{M_2}{EI}. \quad (4b)$$

In (4a) and (4b),  $E$  is the elastic modulus,  $A$  is the cross section area, and  $I$  is the moment of inertia. In addition, the axial strain on the upper surface is given by

$$\varepsilon_{11} = \frac{e - \rho_2 h}{2} \quad (5)$$

where  $h$  is the beam thickness.

The boundary value problem (BVP) of the compliant beam can be written compactly in the following form:

$$\mathbf{X}' = \mathbf{f}(s, \mathbf{X}) \quad (6a)$$

$$\mathbf{g}(\mathbf{X}(0), \mathbf{X}(1)) = \mathbf{0} \quad (6b)$$

where  $\mathbf{X}$  is a vector of the six variables  $(u, w, \theta, F_1, F_3, M_2)^T$ ,  $0 \leq s \leq 1$ , and  $\mathbf{g}(\bullet)$  is the boundary conditions (BCs) specifying the geometrical and/or loading constraints at both ends. The BVP [(6a) and (6b)] can be solved using a MSM [27] given in the Appendix, which recasts the BVP into an initial value problem (IVP).

### B. Boundary Conditions

Appropriate BCs must be specified to solve (3a)–(3f) for the six unknowns in  $\mathbf{X}$  that are physically relevant. Table I summarizes four typical BCs, which are also commonly specified for analyzing columns. For a cantilever (type 1), where the slope and displacements are zeros at the fixed end, the forces and moment at the free end must be specified. For a beam with both ends constrained with pin joints (type 2), the displacement constraints cannot sustain any moment;  $M_2 = 0$  but  $F_1$  must be specified. As will be illustrated, types 3 and 4 are specified for sensor attachment and for negotiating a convex corner, respectively. Type 3 is similar to type 2, but can resist nonzero moments while maintaining zero slopes at both ends. In type 4, a nonzero moment can be exerted against an offset pinned end. Unlike buckling analyses, where the critical load causing a column to buckle is of particular concern, the models developed here relax several commonly made ideal-beam assumptions (such as massless and small deflection) for practical FMN applications.

### C. Illustrative Examples

The beam model is best illustrated by numerically simulating the two basic functions of an existing FMN [5], where a compliant beam connects the front and rear axles of the FMN (see Fig. 1).

- 1) The first function attaches or detaches an accelerometer on/from the surface to be measured. The compliant beam is normally straight. When a measurement is to be made, the front axle is driven toward the rear axle to buckle the compliant beam allowing the accelerometer to be pressed against the surface to be measured.

TABLE I  
 BCs FOR GENERALIZED CONSTRAINTS

Type	1. Cantilever	2. Both ends pinned	3. Slide against a fixed end	4. Slide against an offset pinned end
$s = 0$	$\theta = u = w = 0$	$M_2 = 0, u = w = 0$	$\theta = u = w = 0$	$M_2, u, w$
$s = 1$	$F_1, F_3, M_2$	$F_1, M_2 = 0, w = 0$	$F_1, \theta = w = 0$	$F_1, \theta = w = 0$

2) The second function provides a means to overcome obstacles when moving on a structure. Among the challenges is negotiating sharp corners. Magnetic forces at the corner greatly decrease when negotiating a convex corner but increase (because of multiple contacts) when moving up or down a concave corner.

As illustrated in Fig. 3(a), the FMN consists of two U-shaped structural frames, on which the motors and electronics are housed, and a spring steel (0.254 mm thick) laminate including a compliant beam (shaded in gray). The nonshaded portions are fastened by screws onto the U-shaped frames. The accelerometer (50 g) is pinned in the middle of the beam by screws (at locations shaded in black). The geometrical and mechanical properties of the compliant beam are given in Fig. 3(b). The beam has nonuniform cross sections; thus,  $A$  and  $I$  are functions of  $s$ . Fig. 3(c) shows a steel (A36) structure as the working environment, where the FMN will cross corner A and attach a sensor at B and C.

Numerical simulations using MSM were performed, where computation time (especially when there is buckling) depends on the number of segments  $N$  and initial values for the iterative process. The MSM computation involves a  $6(N+1) \times 6(N+1)$  matrix inverse. To reduce computation time, the beam is equally divided into three segments ( $N = 3$  and  $m = 4$  in Fig. 14) with the beam cross-sectional area presented as a piecewise linear function of path length. As given in Table I, some of the initial values are zeros. The remaining nonzero initial values are determined by physics. Consider a cantilever as an illustration; the values of  $F_1$  and  $F_3$  at  $s = 0$  can be obtained from equilibrium, and  $M_2$  can be chosen as the multiplication of the forces by a characteristic length (such as one half of the beam length).

*Example 1 (Sensor Attachment):* In modeling the sensor attachment on a plane, the rear axle is treated as a fixed end and the front axle acts as a slider subjected to a uniaxial loading  $F_1$ , as shown in Fig. 4. In addition, it is assumed that the compliant beam is constrained to bend only in the  $-z$  direction. For a given wheel radius, the uniaxial loading  $F_1$  required to move the sensor to its desired displacement  $w_s$  (at  $s = 1/2$ ) depends on the direction of the sensor displacement relative to gravity, as compared in Fig. 4, which compares two cases. Unlike case 1, where the weights of the sensor and beam facilitate the sensor attaching, the beam must compensate for these weights in case 2. To explain the effect of the gravity, we normalize the specified  $F_1$  to the critical buckling force for a beam subjected

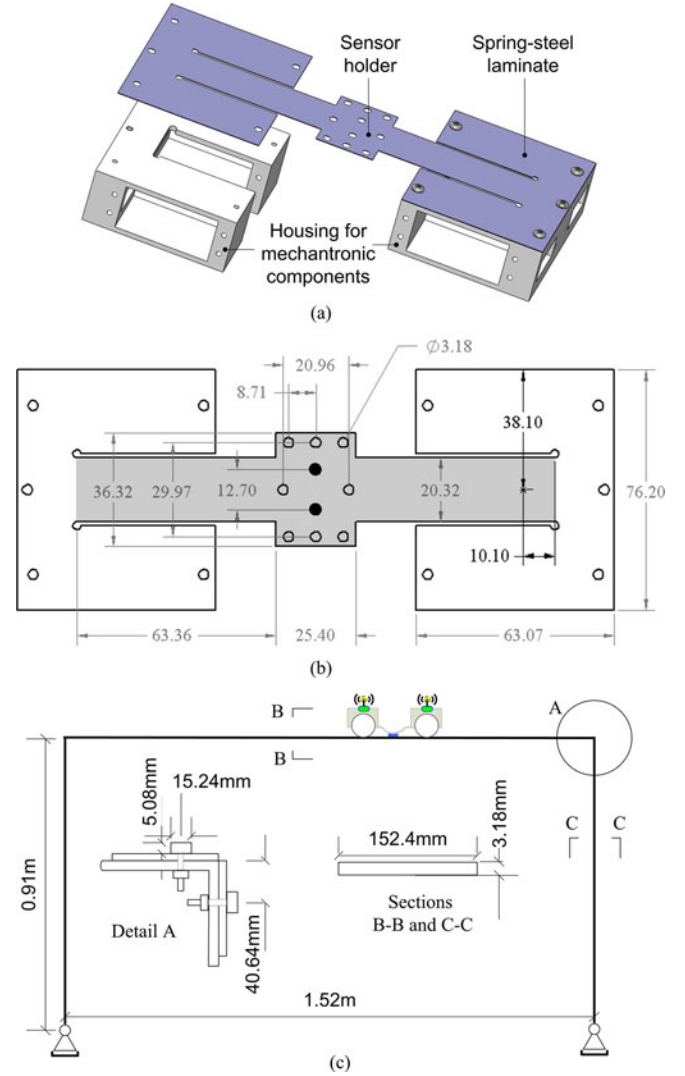


Fig. 3. CAD model of compliant structure for a magnetic FMN. (a) CAD model. (b) Spring-steel laminate. ( $E = 207$  GPa,  $G = 79.3$  GPa, Poisson ratio = 0.3, density = 7.63 g/cm<sup>3</sup>, and thickness = 0.254 mm). (c) Steel (A36) frame structure.

to both ends fixed [33] as follows:

$$n = F_1 \left( \frac{4L^2}{\pi^2 EI_n} \right) \quad (7)$$

where  $I_n$  is the moment of inertia for the narrowest section (width = 20.32 mm in Fig. 3) of the beam, and  $L$  is the beam length. For the sensor, the gravity normalized using (7) is about 0.8. With type-3 BCs, the deformed shape (or  $w$  as a function

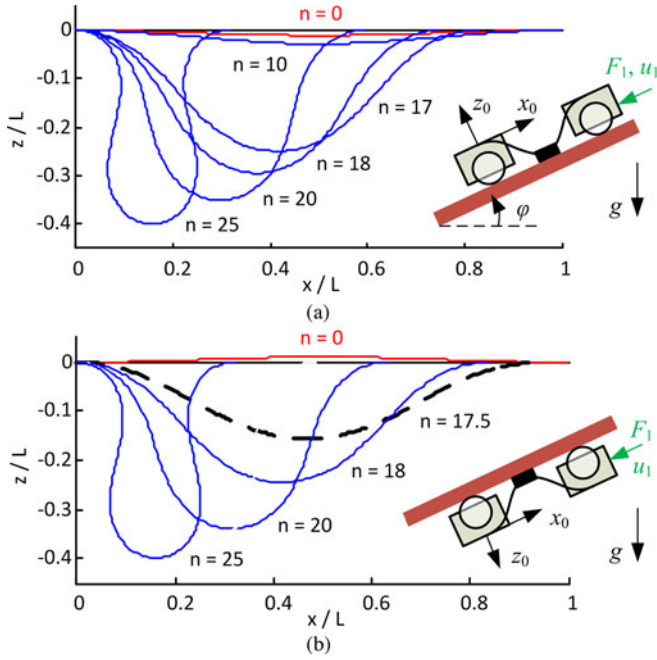


Fig. 4. Effect of gravity. (a) Case 1:  $\varphi = 0$ . (b) Case 2:  $\varphi = 0$ .

of path length  $s$ ) and  $u_1$  for specified  $F_1$  can be computed by solving the BVP (6). The results for the two cases (with  $\varphi = 0$ ) are compared in Figs. 4 and 5, where  $n$  varies from 0 to 25.

Some observations are discussed as follows.

- 1) Figs. 4(a) and 5(a) show that the beam deforms continuously as the normalized force increases in case 1.
- 2) Although the carrying mass (50 g sensor) is relatively light causing negligible deformation under its own weight (see red curves in Fig. 4,  $F_1 = 0$ ), this little weight, however, has a significant buckling effect on the beam in case 2. As illustrated in Figs. 4(b) and 5(a), both the displacements ( $u_1$  and  $w_s$ ) in case 2 do not change until the normalized force exceeds a critical value  $n_c$  at which the beam buckles drastically to a new shape [see black dash curve in Fig. 4(b)] without any intermediate shapes. The values of  $u_1$  and  $w_s$ , which correspond to  $n_c$  for  $\varphi = 0^\circ$ ,  $45^\circ$ , and  $90^\circ$ , are summarized in Table II, which also shows the effects of sensor weights on these values. These critical values that cause buckling to set off in case 2 decrease (requiring less compensation against gravity) as  $\varphi$  increases. For the same reason, a heavier weight tends to give rise to a larger critical value for  $\varphi < 45^\circ$ . On the other hand, a smaller critical value for a heavier weight for  $\varphi > 45^\circ$  is observed as gravity facilitates buckling.
- 3) For  $\varphi = 90^\circ$ , the theoretical value of 16 given in [33] for a weightless beam is somewhat larger than  $n_c$  of 15.5. The beam model given in (3a)–(3f) accounts for the gravity along  $-x$ , which contributes to the onset of buckling.
- 4) The values of  $w_s$  for different  $\varphi$  values converge to the case  $\varphi = 90^\circ$  for large  $F_1$  when the gravity becomes negligible. This is also true for  $u_1$  because of the monotonous relation between  $w_s$  and  $u_1$ , as shown in Fig. 5(b). The maximum normalized force required is  $n = 25$ , from which the re-

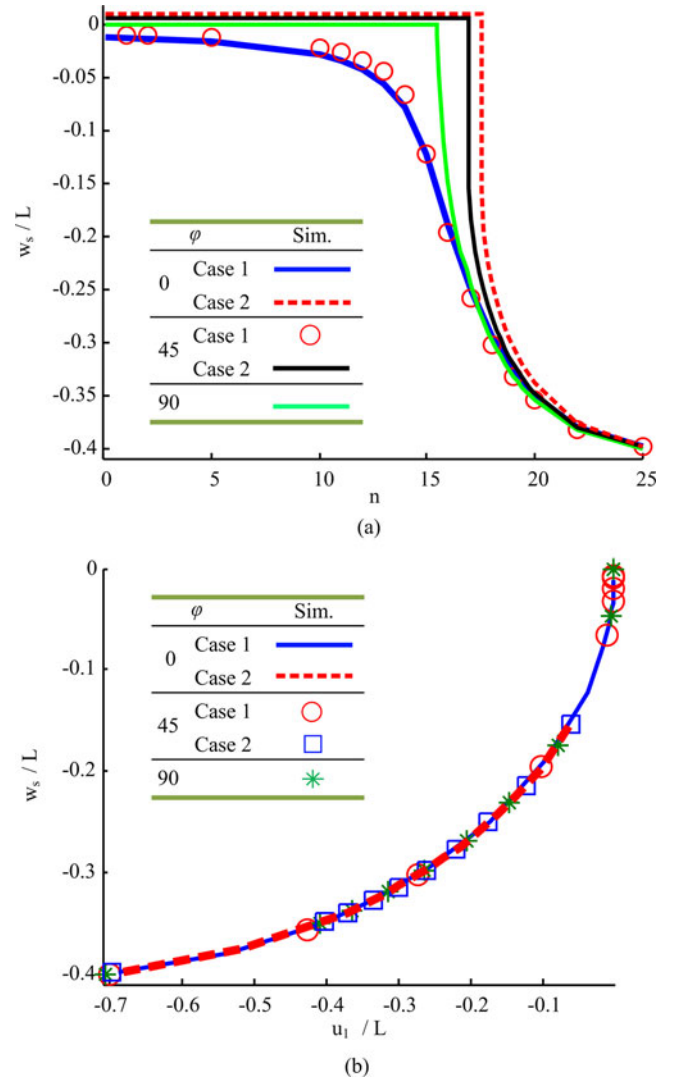


Fig. 5. Relationship between normalized force and displacements. (a) Relation between force  $n$  and displacement  $w_s/L$ . (b) Relation between  $u_1$  and  $w_s$ .

TABLE II  
SLOPE ANGLE AND CRITICAL VALUES

Sensor mass (gram)	$\varphi$ (degree)	$n_c$	$u_1/L$	$w_s/L$
50	0	17.5	-0.0624	0.1559
	45	16.9	-0.0612	0.1543
	90	15.5	-0.0002	0.0094
100	0	18.3	-0.0999	0.1948
	45	17.3	-0.1069	0.2009
	90	15.1	-0.00005	0.0001

quired motor torque can be estimated by multiplying  $F_1$  computed from (7) by the wheel radius  $r_w$ .

- 5) The solution to the beam model provides two alternative manipulating variables ( $F_1$  or  $u_1$ ) of controlling  $w_s$  for attaching a sensor. As illustrated in Fig. 5(a), the relationship between  $F_1$  and  $w_s$  is not only highly nonlinear, but also depends on  $\varphi$ . On the other hand, the relationship between  $w_s$  and  $u_1$  is monotonically smooth and independent of  $\varphi$ , as shown in Fig. 5(b). Thus, it is a preferable variable for

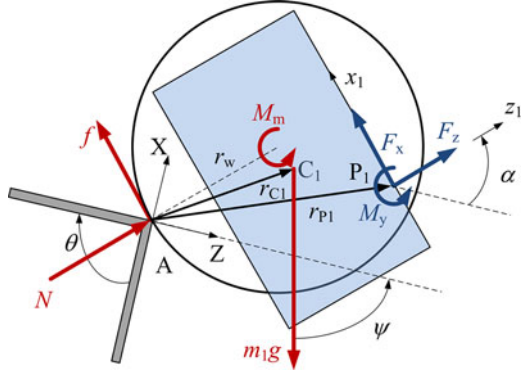


Fig. 6. Convex corner negotiation.

controlling the compliant beam of the FMN by manipulating the input displacement  $u_1$  rather than the input force  $F_1$ . For the compliant design given in Fig. 3, the inverse model that computes  $u_1$  for a specified  $w_s$  for attaching sensor is given by curve fitting the data in Fig. 5(b) for different  $\varphi$ 's in both cases

$$\frac{u_1}{L} = 18 \left( \frac{w_s}{L} \right)^3 + 5.3 \left( \frac{w_s}{L} \right)^2 - \frac{0.85w_s}{L}. \quad (8)$$

This result is due to the lightweight of the combined beam and sensor. For detaching a sensor, the command becomes  $-u_1$  for a reversed process.

*Example 2 (Convex Corner Negotiation):* Fig. 6 shows the free body diagram of the front assembly (mass  $m_1$  at mass center  $C_1$  and wheel radius  $r_w$ ) at an instant crossing a convex corner A. The reference  $OXYZ$  is defined such that  $X$  is on the plane, where the FMN initially locates and points in the moving direction before crossing the corner, and  $Z$  is normal to the plane. In Fig. 6,  $\psi$  is the angle between  $Z$  and the gravity,  $N$  is the reaction force,  $f (= \mu N)$  is the friction,  $\mu$  is the coefficient of friction between the wheel and surface, and  $M_m$  is the torque provided by the motors. The following assumptions are made in this discussion.

- 1) The wheels are designed with magnets such that they attach on the steel surfaces as the FMN moves.
- 2) The motor torque satisfying the nonslip condition:  $M_m = fr_w \leq \mu N(\alpha)r_w$ .
- 3) The moment due to the magnets is small as compared to that due to gravity, and thus, neglected in the analysis.

The following discussion considers a worst scenario, where the wheel has a point contact at the corner. The strategy for an FMN to negotiate a convex corner comprises three steps.

*Step 1:* The rear axle exerts forces/torque ( $F_x$ ,  $F_z$ , and  $M_y$ ) through the compliant beam to rotate the front axle about A.

*Step 2:* As soon as the front axle crosses over the corner ( $\alpha = \theta$ , where  $\theta$  is the corner angle), the two assemblies move together.

*Step 3:* Once the rear axle arrives at the corner, the front axle pulls it over via the compliant beam.

The following details step 1 as this initiation dictates the success of the corner negotiation. Fig. 7 shows the beam de-

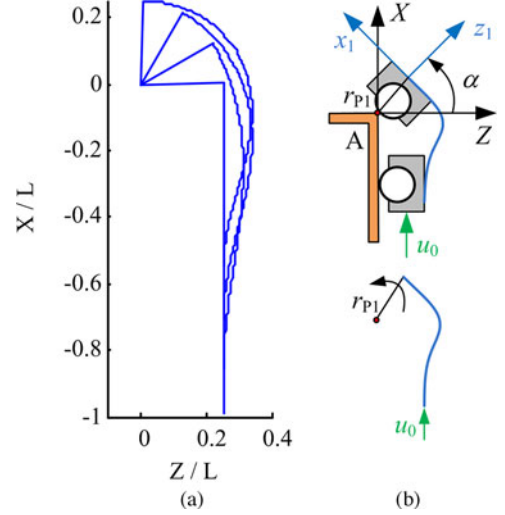


Fig. 7. Simulation of corner negotiation. (a) Beam deformations. (b) Coordinates.

formations as the front assembly crosses the corner. As will be shown, the other steps follow similar principles.

To rotate the front assembly over the corner, the following condition (9) with respect to A must be satisfied:

$$M_r \mathbf{i}_y + \mathbf{r}_{C_1} \times m_1 \mathbf{g} \geq 0 \quad (9)$$

where  $M_r \mathbf{i}_y = \mathbf{r}_{P_1} \times (F_x \mathbf{i}_{x_1} + F_z \mathbf{i}_{z_1}) + M_y \mathbf{i}_y$  is the required moment to compensate for the torque due to gravity, and is shown in Fig. 8 for different  $\psi$  values. For negative  $\psi$ ,  $M_r$  can be obtained from the mirror images of Fig. 8. Since the compliant beam attaches the front assembly at  $P_1$

$$F_x = -F_1 \quad (10a)$$

$$F_z = -F_3 \quad (10b)$$

$$M_y = -M_2. \quad (10c)$$

The BCs ( $M_2$ ,  $u$ , and  $w$ ) for negotiating a convex corner, which take the form of type 4 in Table I, can be obtained from (11) and (12)

$$M_2 = -\mathbf{r}_{P_1} \cdot (F_1 \mathbf{i}_{z_1} - F_3 \mathbf{i}_{x_1}) - M_r \quad (11)$$

$$[u \quad w] = [\mathbf{i}_X \quad \mathbf{i}_z] \begin{bmatrix} \cos \alpha & -\sin \alpha \\ \sin \alpha & \cos \alpha \end{bmatrix} \mathbf{r}_{P_1}. \quad (12)$$

Solving (3a)–(3f) with (11) and (12) as constraints using MSM, the simulation results are given in Fig. 8 showing the relation between  $\alpha$  and the applied force (for  $\psi$  equal to 0,  $\pm\pi/4$ ,  $\pm\pi/2$ ), which are highly nonlinear. The larger the  $\psi$ , the larger the force required for a desired rotation angle, and the maximum normalized force is about 4.5 (smaller than the maximum force of 25 for sensor attachment).

### III. EXPERIMENTAL RESULTS AND DISCUSSION

A prototype FMN that has two (front and rear) wheel assemblies is shown in Fig. 9(a). Each assembly has a pair of

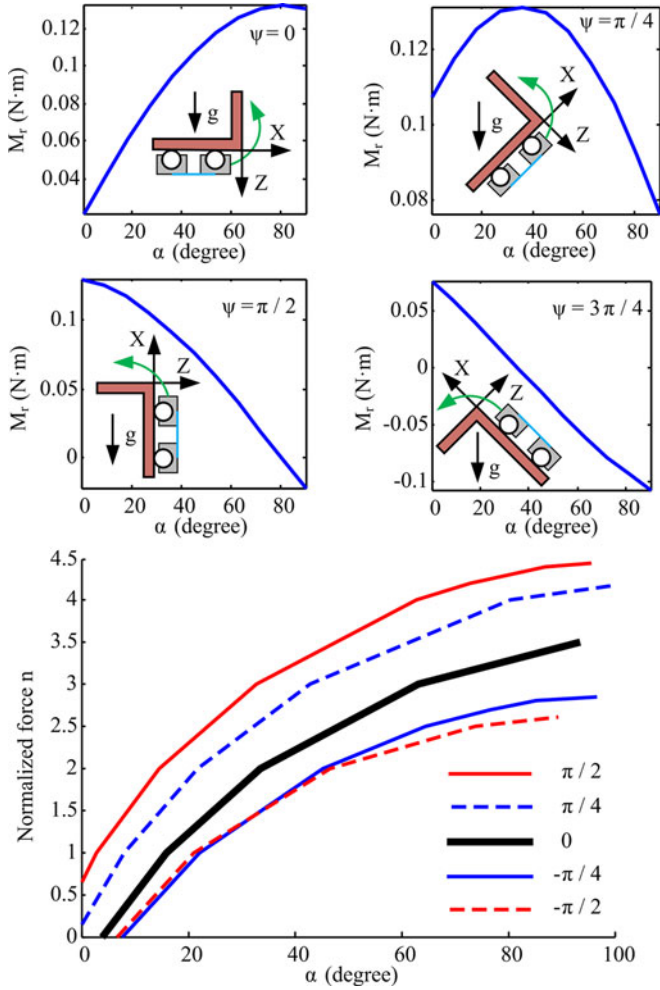


Fig. 8. Relation between rotation angle  $\alpha$  and normalized force  $n$ .

magnetic wheels (independently driven by electric motors), a microprocessor-based pulse width modulation controller, and wireless communication circuits. The overall weight of the FMN is 1 kg contributed primarily by the magnets, motors, and batteries. Details of the frame structure and compliant beam are given in Fig. 3(a) and (b). The beam is mainly designed to attach/detach an accelerometer [see Fig. 9(b) and (c)] by bending, as well as negotiate corners [see Fig. 9(d) and (e)] and reinforcement ridges [see Fig. 9(f)]. Although the beam can be subjected to some limited twisting that would allow the FMN to move out-of-plane to another surface, as illustrated in Fig. 9(g) and (h), results discussed here focus on two functional examples (see Section II) that require only 2-D bending.

The objectives of the experiments are as follows.

- 1) The first objective is to validate the beam model (that reduces the problem from 2-D to 1-D, depending only on the path length  $s$ ) by comparing against experiments and those computed using FEM. To achieve this objective, the spring-steel laminate alone was used (with one U-shape frame for fixation) so that the complexities of the front and rear assemblies can be avoided.

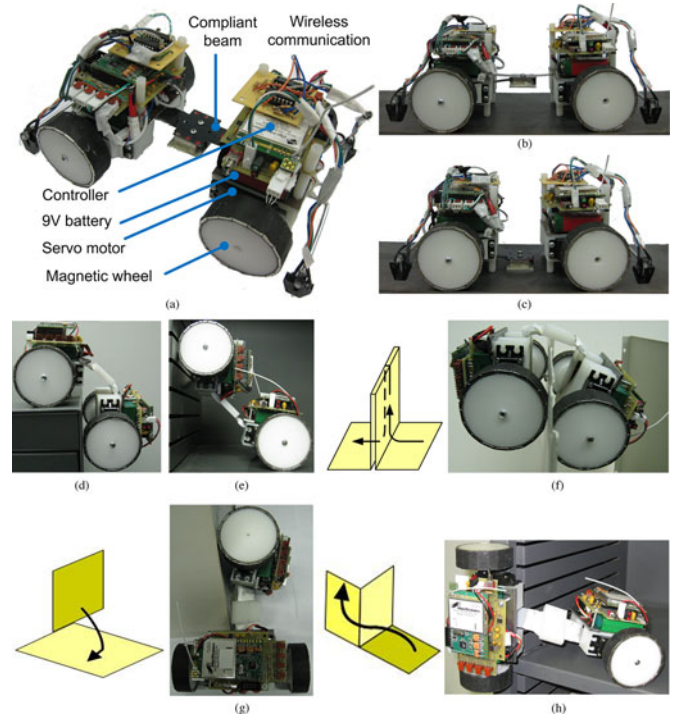


Fig. 9. Prototype FMN. (a) Prototype FMN. (b) Not buckled. (c) Buckled. (d) Convex corner. (e) Concave corner. (f) Crossing reinforced ridge. (g)  $90^\circ$  twisting to another surface. (h) Twist/bend onto different surfaces.

- 2) The second objective is to investigate the effect of gravity on sensor attachment by comparing simulations for the structure at  $\varphi = 0$  and  $90^\circ$  [see Fig. 5(b)] against those obtained experimentally. The comparison also provides a basis for validating (8) that relates the displacement  $w_s$  (for attaching a sensor) to the input displacement  $u_1$ .
- 3) The third objective is to examine the effectiveness of the proposed strategy for crossing a corner. Of particular interest is to determine the required input displacement  $u_0$  for a desired rotation angle  $\alpha$ , as shown in Fig. 7.

For quantitative comparison, experimental results of the sensor attachment and corner negotiation processes were computed from images filmed by a camcorder (Sony HDR-SR11).

#### A. Validation of the Beam Model

Fig. 10(a) shows the experimental setup to examine the validity of the beam model, where the spring-steel laminate on one of two housing structures [see Fig. 3(a)] was clamped as a cantilever, and thus, has type 1 constraints (see Table I). The remaining U-shaped portion [see nonshaded area in Fig. 3(b)] in the spring-steel laminate serves as a load at the end of the compliant beam (that has a nonuniform shape and thus nonuniform distributed weight). As the mass center of this U-shaped portion is located at 10.1 mm from the free end of the beam [see Fig. 3(b)], the weight of this U-shaped portion also contributes to a lateral force  $F_U$  and a moment  $M_U$  in addition to the external payload  $m_p$  at the free end of the beam. As a result, the

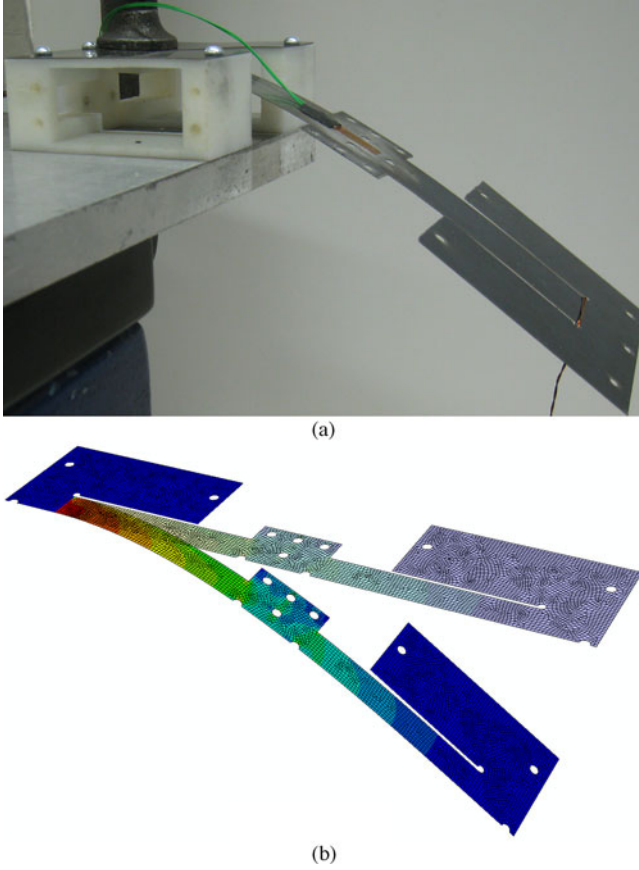


Fig. 10. Validation of beam model. (a) Experiment setup. (b) Finite-element analysis.

values of  $F_1$ ,  $F_3$ , and  $M_2$  in the BCs are given by

$$F_1 = 0 \quad F_3 = F_U + m_p g \quad M_2 = M_U. \quad (13)$$

In this experiment, a strain gauge (with negligible weight as compared to the beam) was attached on the upper surface at the middle of the beam. To provide an alternative basis for comparisons, a numerical model was built in Abaqus using 6319 shell elements (S4R type). In finite element analysis, only one-half of the beam is simulated because of symmetry, and the external load is applied at one coupling element so that  $F_U$  is uniformly distributed over the cross section at the beam tip. All computations were performed on a computer with a 2.99-GHz CPU and 4.00 GB memory; the FEM took about 365 s, while the beam model (three-segment MSM) requires only 95 s. The results are given in Fig. 11, which compares the results of two beam models, uniform width of 20.32 mm and nonuniform shape (that accounts for the geometry of the sensor holder), against those of FEM and experiment.

The results are discussed as follows.

- 1) Fig. 11(a) shows that the FEM-computed beam shapes and the uniform/nonuniform beam models closely agree with each other for two different loadings; external payload  $m_p = 0$  and 50 grams exerted at the beam tip.
- 2) Fig. 11(b) shows that the strain  $\varepsilon_{11}$  increases monotonically with payload. The beam model agrees well with the

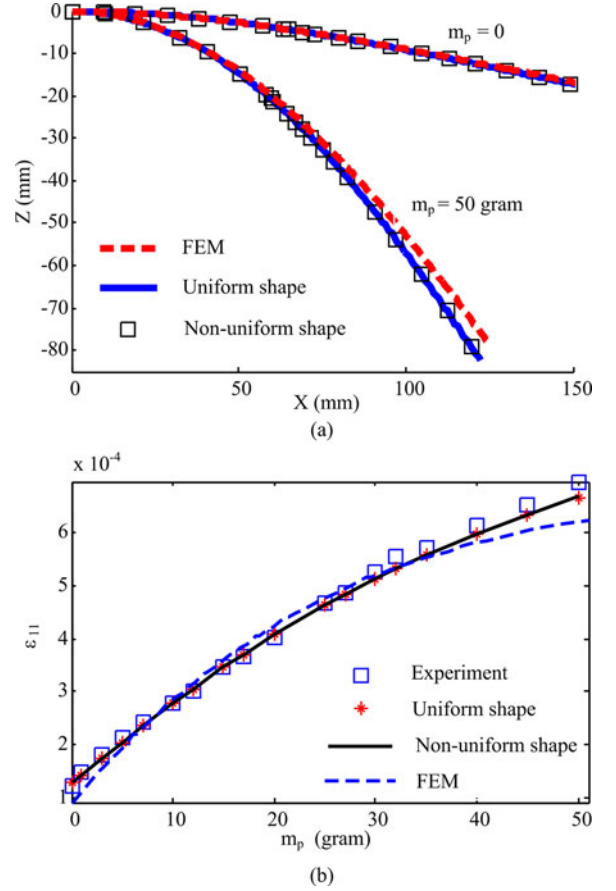


Fig. 11. Comparison of results. (a) Comparison of deformed shapes. (b) Comparison of upper surface strains at the middle of the beam.

experimental measurements. Some discrepancies at large payloads are observed in FEM possibly due to the following local effects.

- a) Because of FE meshes, the node at which strain information is extracted does not locate exactly at the middle of the beam.
- b) Besides, the FEM model can capture the local stress concentration while the strain gauge is actually measuring the average strain over its area, and the stress concentration is not accounted in this beam model. When comparing this local information, the beam model matches with experiments, but some discrepancy exists in the FEM.

It is noted that the ten-hole area takes up to 8% of that of the sensor holder, which was compensated for by a function characterizing the change in beam widths; thus, the results from two beam models, uniform and nonuniform shapes, do not differ significantly in this specific application.

### B. Effect of Gravity on Sensor Attachment

In this experiment, the sensor was attached on the plane by moving both axes toward each other to prevent slippage, as shown in Fig. 12(a)–(c). For comparing against analytical simulations, where sensor attachments were modeled as a process

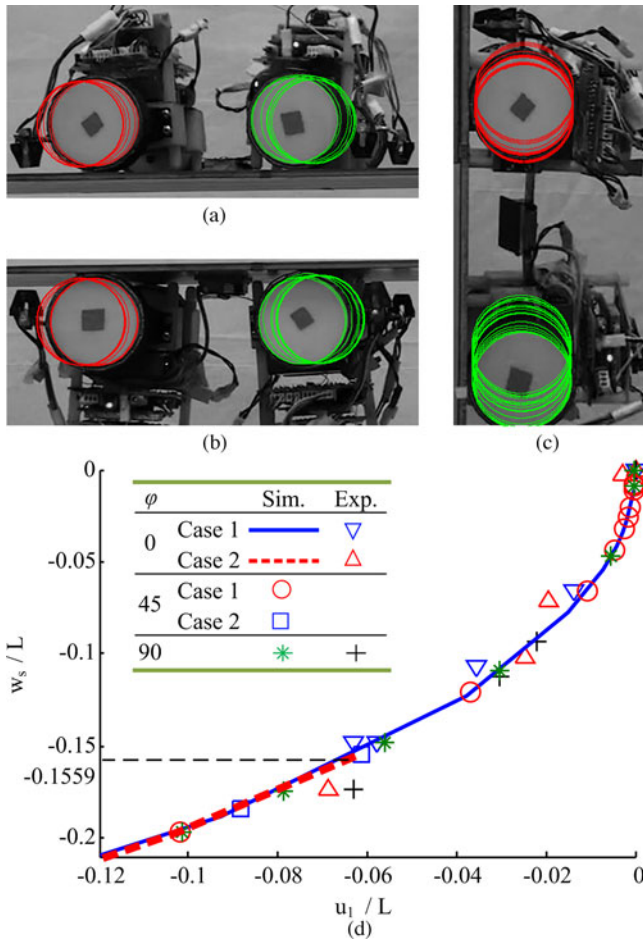


Fig. 12. Sensor attachment. (a) Case 1:  $\varphi = 0$ . (b) Case 2:  $\varphi = 0$ . (c)  $\varphi = 90^\circ$ . (d) Displacement comparison between simulation and experiment.

of moving the front axle toward the fixed rear axle, the net displacement  $u_1$  was obtained by measuring the distance change between the front and rear wheel centers from captured images.

Fig. 12(d) is a zoom-in comparison of Fig. 5(b) showing good agreements between analyses and experiment results for  $\varphi = 0$ ,  $45^\circ$ , and  $90^\circ$ . It is worth noting that the deviation in case 2 for  $\varphi = 0$  was a result of the onset of buckling; once the critical force is overcome,  $w_s/L$  jumps from zero to  $-0.1559$ . This nonlinear dynamic is essentially unstable. Thus, in case 2, the required input displacement  $u_1$  for  $w_s/L > -0.1559$  is of the same value ( $u_1/L = -0.06$ ) as that when buckling starts. However, all the intermediate experiment data follows the continuous curve given by (8), which is independent of slope angle  $\varphi$ ; therefore, the relation between  $u_1$  and  $w_s$  obtained from static analysis is also valid for the dynamic process of case 2. This also justifies for the conclusion obtained from Fig. 5 to control the compliant beam deformation by manipulating the input displacement  $u_1$  rather than the input force  $F_1$ .

### C. Validation of the Corner Negotiation

Fig. 13(a)–(c) shows the three steps in negotiating a convex right corner by pushing the front axle, both axles moving together, and finally pulling the rear axle. Following the earlier

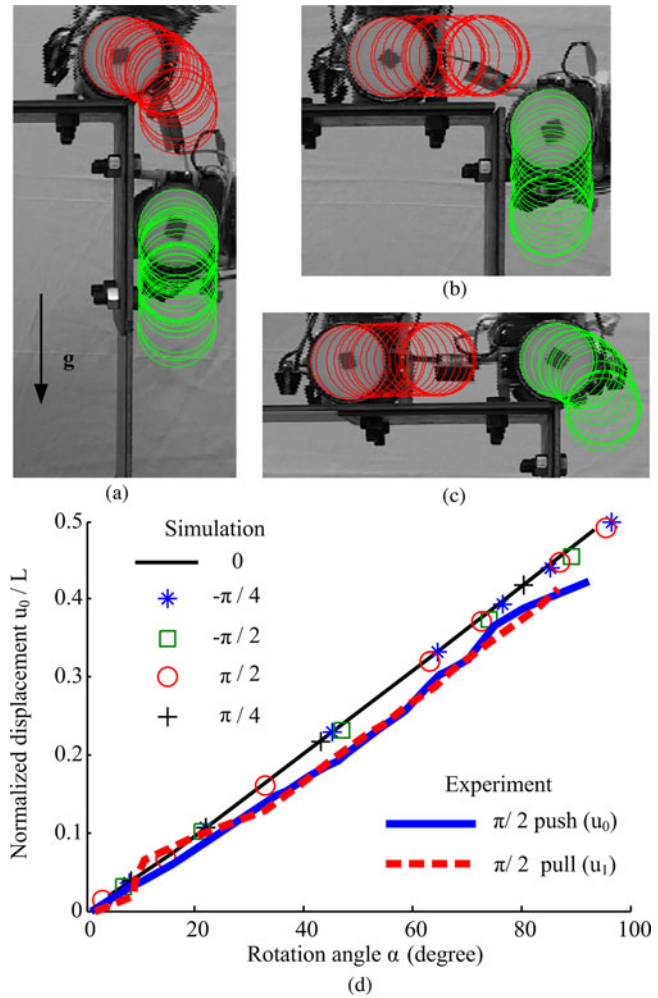


Fig. 13. Convex right corner negotiation. (a) Push the front axle. (b) Move together. (c) Pull the rear axle. (d) Relation between rotation angle  $\alpha$  and displacement  $u_0/L$ .

analysis, the rotation angle  $\alpha$  of the front axle is obtained by the orientation of the line connecting the front wheel center and the corner point, while the displacement  $u_0$  of the rear axle is determined by the rear wheel center. Although the relation between the applied force  $F_1$  and the desired rotation angle  $\alpha$  is nonlinear, depending on the gravity direction, a highly linear relation  $u_0/L = 0.0051\alpha$  exists between  $u_0$  and  $\alpha$  regardless of the gravity direction in simulation, as shown in Fig. 13(d). Experiment results also confirm with this linear relation. It is noted that errors may come from the required torque that is calculated from the assembly mass and the distance from the corner to the mass center. Another source of error can be the image processing of the video frames when detecting the front and rear axle locations by wheel centers, and determining the corner point by manually picking one pixel. Since the steel structure and the camcorder are fixed throughout the experiment, this corner point A is fixed in all the images, while small vibration can exist in the steel structure because of the FMN dynamics. It can also be seen that both the pushing and pulling processes follow the same curve in experiment, implying that the aforementioned analysis for

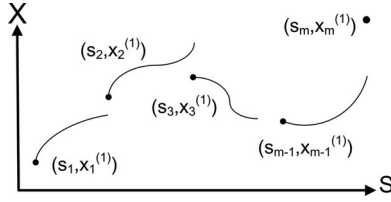


Fig. 14. Multiple shooting method.

the pushing process (see step 1) can be applied throughout the corner negotiation.

#### IV. CONCLUSION

Along with an analytical model for simulating the large deformation of a compliant beam in 2-D space, a magnetic FMN incorporating a compliant mechanism has been designed to negotiate corners and carry a sensor for placing on a ferromagnetic structure. Two illustrative examples of sensor attachment and corner negotiation are presented for different constraints for the same mechanical design of FMN. Simulation results show that there exist consistent relations between input/output displacements and rotation angle for control implementation in sensor attachment and corner negotiation, regardless of gravity direction. In sensor attachment, a nonlinear relation between the front assembly displacement and the sensor displacement is valid for different critical forces for buckling, which is affected by the working surface slope. In corner negotiation, a linear relation can be obtained between the displacement of the rear assembly and the rotation angle of the front assembly within the highly nonlinear load-displacement behaviors of a compliant beam. However, the gravity affects the loading and displacement/rotation angle relation. To set off the beam buckling for the sensor attachment, the smaller the surface slope angle, the larger the critical force needed; a heavier sensor weight tends to give rise to a larger critical force for slope angle  $\varphi \leq 45^\circ$  while smaller critical force for  $\varphi > 45^\circ$ . For a desired rotation angle in corner negotiation, a larger pushing force is required with a larger angle  $\psi$  between the gravity and the norm of the initial plane. The analytical model is validated by an experiment on a cantilever beam and the corresponding finite-element model. Finally, the experimental results of two functionalities of sensor attachment and corner negotiation are provided to validate the simulation analysis.

#### APPENDIX

##### MULTIPLE SHOOTING METHOD

The BC problem (BVP) of a 2-D compliant beam can be written in the following form:

$$\mathbf{X}' = \mathbf{f}(s, \mathbf{X}) \quad \mathbf{g}(\mathbf{X}(0), \mathbf{X}(L)) = 0 \quad (\text{A1})$$

where  $\mathbf{X}$  is a vector of the six variables,  $0 \leq s \leq 1$ , and  $\mathbf{g}(\bullet)$  is the BCs specifying the geometrical loading constraints at both ends. The BVP (A1) is recast as an IVP and solved using an MSM [27]. For this, the region  $[0, 1]$  is divided into  $m - 1$  sections by  $m$  nodes, as shown in Fig. 14, where  $s_i$  is the arc

length from the root of the beam to the  $i$ th node,  $x_i^{(n)}$  is the initial guesses for the  $i$ th section, and the superscript  $(n)$  denotes the  $n$ th guess.

The BVP can then be posed as a set of  $m$  first-order nonlinear equations (A2) subject to a set of  $m$  constraints (A3) as functions of the initial guesses

$$\mathbf{X}' = \mathbf{f}(s, \mathbf{X}) \quad \mathbf{X}(s_i) = \mathbf{x}_i^{(n)} \quad (\text{A2})$$

$$\mathbf{C}(\mathbf{x}^{(n)}) := \begin{bmatrix} \mathbf{C}_1(\mathbf{x}_1^{(n)}, \mathbf{x}_2^{(n)}) \\ \vdots \\ \mathbf{C}_{m-1}(\mathbf{x}_{m-1}^{(n)}, \mathbf{x}_m^{(n)}) \\ \mathbf{C}_m(\mathbf{x}_1^{(n)}, \mathbf{x}_m^{(n)}) \end{bmatrix} := \begin{bmatrix} \mathbf{X}(s_2; s_1, \mathbf{x}_1^{(n)}) - \mathbf{x}_2^{(n)} \\ \vdots \\ \mathbf{X}(s_m; s_{m-1}, \mathbf{x}_{m-1}^{(n)}) - \mathbf{x}_m^{(n)} \\ \mathbf{g}(\mathbf{x}_1^{(n)}, \mathbf{x}_m^{(n)}) \end{bmatrix}. \quad (\text{A3})$$

Using the Newton method, the initial guesses are updated using (A4)

$$\mathbf{x}^{(n+1)} = \mathbf{x}^{(n)} - \alpha [\mathbf{DC}(\mathbf{x}^{(n)})]^{-1} \mathbf{C}(\mathbf{x}^{(n)}), \quad n = 0, 1, \dots \quad (\text{A4})$$

where  $\mathbf{DC} = \partial \mathbf{C} / \partial \mathbf{x}^{(n)}$  is a matrix, and  $\alpha$  is a coefficient for the iteration step size. The iteration process of (A4) stops until  $\mathbf{C}(\mathbf{x}^{(n)}) \rightarrow \mathbf{0}$  (or a small tolerance error  $\text{Err}_{\text{tol}}$ ), implying that the solution is continuous and satisfies the BCs. The MSM can be implemented using the following steps:

- 1) set the initial guess  $\mathbf{x}^{(0)} = [\mathbf{x}_1^{(0)} \quad \mathbf{x}_2^{(0)} \quad \dots \quad \mathbf{x}_m^{(0)}]$ ;
- 2) solve the IVP (9a) with  $\mathbf{X}(0) = \mathbf{x}^{(0)}$ ;
- 3) calculate the residual  $\|\mathbf{C}(\mathbf{x}^{(0)})\|$  and corresponding  $\mathbf{DC} = \partial \mathbf{C} / \partial \mathbf{x}^{(0)}$ ;
- 4) update the initial guess by (A4);
- 5) repeat steps 2–4 (replacing  $\mathbf{x}^{(0)}$  with  $\mathbf{x}^{(n)}$ ) until  $\|\mathbf{C}(\mathbf{x}^{(n)})\| < \text{tolerance error } \text{Err}_{\text{tol}}$ .

#### REFERENCES

- [1] J. P. Lynch and K. J. Loh, "A summary review of wireless sensors and sensor networks for structural health monitoring," *Shock Vib. Dig.*, vol. 38, no. 2, pp. 91–128, 2006.
- [2] I. F. Akyildiz, W. Su, Y. Sankarasubramaniam, and E. Cayirci, "A survey on sensor networks," *IEEE Commun. Mag.*, vol. 40, no. 8, pp. 102–144, Aug. 2002.
- [3] K.-M. Lee, Y. Wang, D. Zhu, J. Guo, and X. Yi, "Flexure-based mechatronic mobile sensors for structure damage detection," presented at the 7th Int. Workshop Struct., Health Monitoring, Stanford, CA, 2009.
- [4] J. Guo, K.-M. Lee, D. Zhu, and Y. Wang, "A flexonic magnetic car for ferro-structural health monitoring," presented at the ASME Dyn. Syst. Control Conf., Hollywood, CA, 2009.
- [5] D. Zhu, X. Yi, Y. Wang, K.-M. Lee, and J. Guo, "A mobile sensing system for structural health monitoring: Design and validation," *Smart Mater. Struct.*, vol. 19, 055011, 2010.
- [6] J. Z. Shang, T. Sattar, S. Chen, and B. Bridge, "Design of a climbing robot for inspecting aircraft wings and fuselage," *Int. J. Ind. Robot.*, vol. 34, pp. 495–502, 2007.
- [7] S. C. Han, J. Kim, and H. C. Yi, "A novel design of permanent magnet wheel with induction pin for mobile robot," *Int. J. Precision Eng. Manuf.*, vol. 10, no. 4, pp. 143–146, 2009.

- [8] H. Yaguchi and N. Sato, "Globular magnetic actuator capable of free movement in a complex pipe," *IEEE Trans. Magn.*, vol. 46, no. 6, pp. 1350–1355, Jun. 2010.
- [9] H. Wei, Y. Chen, J. Tan, and T. Wang, "Sambot: A self-assembly modular swarm robot system," *IEEE/ASME Trans. Mechatronics*, Nov. 11, 2010.
- [10] S. Liu, D. Sun, and C. Zhu, "Coordinated motion planning for multiple mobile robots along designed paths with formation requirement," *IEEE/ASME Trans. Mechatronics*, Sep. 23, 2010.
- [11] H. Mehrjerdi, M. Saad, and J. Ghommam, "Hierarchical fuzzy cooperative control and path following for a team of mobile robots," *IEEE/ASME Trans. Mechatronics*, Jul. 23, 2010.
- [12] F. Tâche, W. Fischer, G. Caprari, R. Siegwart, R. Moser, and F. Mondada, "Magnebike: A magnetic robot with high mobility for inspecting complex shaped structures," *J. Field Robot.*, vol. 26, pp. 453–476, 2009.
- [13] M. Filipovic and M. Vukobratovic, "Expansion of source equation of elastic line," *Robotica*, vol. 26, pp. 739–751, 2008.
- [14] J. G. Garcia, A. Robertsson, J. G. Ortega, and R. Johansson, "Sensor fusion for compliant robot motion control," *IEEE Trans. Robot.*, vol. 24, no. 2, pp. 430–441, 2008.
- [15] U.-X. Tan, W. T. Latt, C. Y. Shee, and W. T. Ang, "A low-cost flexure-based handheld mechanism for micromanipulation," *IEEE/ASME Trans. Mechatronics*, Sep. 27, 2010.
- [16] C.-C. Lan, C.-M. Lin, and C.-H. Fan, "A self-sensing microgripper module with wide handling ranges," *IEEE/ASME Trans. Mechatronics*, vol. 16, no. 1, pp. 141–150, 2011.
- [17] H. Xie and S. Regnier, "Development of a flexible robotic system for multiscale applications of micro/nanoscale manipulation and assembly," *IEEE/ASME Trans. Mechatronics*, vol. 16, no. 2, pp. 266–276, 2011.
- [18] S. K. Dwivedy and P. Eberhard, "Dynamic analysis of flexible manipulators—A literature review," *Mechanism Mach. Theory*, vol. 41, no. 7, pp. 749–777, 2006.
- [19] M. A. Arteaga and B. Siciliano, "On tracking control of flexible robot arms," *IEEE Trans. Autom. Control*, vol. 45, no. 3, pp. 520–527, Mar. 2000.
- [20] G. J. M. Tuijthof and J. L. Herder, "Design, actuation and control of an anthropomorphic robot arm," *Mechanism Mach. Theory*, vol. 35, no. 7, pp. 945–962, 2000.
- [21] L. Gaudiller and F. Matchard, "A nonlinear method for improving the active control efficiency of smart structures subjected to rigid body motions," *IEEE/ASME Trans. Mechatronics*, vol. 12, no. 5, pp. 542–548, Oct. 2007.
- [22] C. La-orpacharapan and L. Y. Pao, "Fast and robust control of systems with multiple flexible modes," *IEEE/ASME Trans. Mechatronics*, vol. 10, no. 5, pp. 521–534, Oct. 2005.
- [23] R. Caracciolo and A. Trevisani, "Simultaneous rigid-body motion and vibration control of a flexible four-bar linkage," *Mechanism Mach. Theory*, vol. 36, no. 2, pp. 221–243, 2001.
- [24] A. Trevisani and M. E. Valcher, "An energy-based adaptive control design technique for multibody-mechanisms with flexible links," *IEEE/ASME Trans. Mechatronics*, vol. 10, no. 5, pp. 571–580, Oct. 2005.
- [25] R. Frisch-Fay, *Flexible Bars*, Washington, D.C.: Butterworths, 1962.
- [26] P. F. Pai and A. H. Nayfeh, "A fully nonlinear-theory of curved and twisted composite rotor blades accounting for warpings and 3-dimensional stress effects," *Int. J. Solids Struct.*, vol. 31, no. 9, pp. 1309–1340, 1994.
- [27] J. Stoer and R. Bulirsch, *Introduction to Numerical Analysis*, 2nd ed. New York: Springer-Verlag, 1980, pp. 476–477.
- [28] P. F. Pai and A. N. Palazotto, "Large-deformation analysis of flexible beams," *Int. J. Solids Struct.*, vol. 33, no. 9, pp. 1335–1353, 1996.
- [29] J. N. Goodier, "Torsional and flexural buckling of bars of thin-walled open section under compressive and bending loads," *J. Appl. Mech., ASME*, vol. 64, pp. A103–A107, 1942.
- [30] S. P. Timoshenko and J. M. Gere, *Theory of Elastic Stability*, 2nd ed. New York: McGraw-Hill, 1961.
- [31] F. S. M. Jarrar and M. N. Hamdan, "Nonlinear vibrations and buckling of a flexible rotating beam: A prescribed torque approach," *Mechanism Mach. Theory*, vol. 42, no. 8, pp. 919–939, 2007.
- [32] J. L. Batoz and G. Dhatt, "Incremental displacement algorithms for nonlinear problems," *Int. J. Numer. Methods Eng.*, vol. 14, pp. 1262–1267, 1979.
- [33] J. M. Gere and S. P. Timoshenko, *Mechanics of Material*, 4th ed. Boston, MA: PWS Publishing, 1997.

**Jiajie Guo** (S'07) received the B.S. degree from the Department of Engineering Mechanics and Science, Peking University, Beijing, China, in 2006, and the M.S. degree in mechanical engineering from the Georgia Institute of Technology, Atlanta, in 2009, where he is currently working toward the Ph.D. degree in mechanical engineering.

His current research interests include compliant mechanisms, mechatronics, and system dynamics/control.

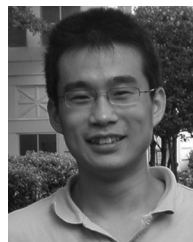
Mr. Guo is a student member of the America Society of Mechanical Engineers.



**Kok-Meng Lee** (M'89–SM'02–F'05) received the B.S. degree from the State University of New York, Buffalo, in 1980, and the S.M. and Ph.D. degrees from the Massachusetts Institute of Technology, Cambridge, in 1982 and 1985, respectively.

He is currently a Professor in the Woodruff School of Mechanical Engineering, Georgia Institute of Technology, Atlanta. He is the holder of eight patents on machine vision, a 3 DOF spherical motor/encoder, and a live-bird handling system. His research interests include system dynamics/control, robotics, automation, and mechatronics.

Dr. Lee is a Fellow of the America Society of Mechanical Engineers. He is the recipient of the National Science Foundation Presidential Young Investigator Award, Sigma Xi Junior Faculty Research Award, International Hall of Fame New Technology Award, and Kayamori Best Paper Award.



**Dapeng Zhu**, received the B.S. degree in civil engineering and the M.S. degree in engineering mechanics from Tsinghua University, Beijing, China, in 2005 and 2008, respectively. He is currently working toward the Ph.D. degree in civil engineering at the Georgia Institute of Technology, Atlanta.

His current research interests include wireless sensor networks, smart materials, and structures.



**Xiaohua Yi** received the B.Sc. degree in civil engineering from Zhejiang University, Zhejiang, China, in 2006. He is currently working toward the Ph.D. degree in the School of Civil and Environmental Engineering, Georgia Institute of Technology, Atlanta.

His current research interests include wireless sensor networks, smart materials, and structures.



**Yang Wang** received the M.S. degree in electrical engineering and the Ph.D. degree in civil engineering, both in 2007 from Stanford University, Stanford, CA.

He is currently an Assistant Professor in the School of Civil and Environmental Engineering, Georgia Institute of Technology, Atlanta. He has published one book chapter and over 60 articles in journals and conference proceedings. His research interests include structural health monitoring and damage detection, decentralized structural control, smart materials and structures, wireless sensor networks, structural dynamics, and earthquake engineering.

materials and structures, wireless sensor networks, structural dynamics, and earthquake engineering.